

Ultimate Control over Hydrogen Bond Formation and Reaction Rates for Scalable Synthesis of Highly Crystalline vdW MOF Nanosheets with Large Aspect Ratio

Yuxia Shen, Bohan Shan, Hui Cai, Ying Qin, Ashutosh Agarwal, Dipesh B. Trivedi, Bin Chen, Lei Liu, Houlong Zhuang, Bin Mu,* and Sefaattin Tongay*

Large-scale synthesis of van der Waals (vdW) metal–organic framework (MOF) nanosheets with controlled crystallinity and interlayer coupling strength is one of the bottlenecks in 2D materials that has limited its successful transition to large-scale applications. Here, scalable synthesis of mBDC ($m = \text{Zn}$ and Cu) 2D MOFs at large scales through a biphasic method is demonstrated. The results show replacing water molecules with pyridine eliminates hydrogen bond formation at metal cluster sites. This prohibits tight coupling across adjacent MOF layers and sustains controllable 2D vdW MOF growth. It is further shown that control over the growth speed, crystallinity, and thickness can be achieved by addition of a controlled amount of triethylamine and formic acid to achieve highly crystalline vdW MOF nanosheets with extraordinarily high aspect ratio. The described synthesis route can easily be scaled up for large-scale production either by deposition onto desired substrates or in crystalline layered powder form. Owing to its large lateral size, vdW nature, and high crystallinity, it is possible to perform atomic force microscopy, Kelvin probe force microscopy, and Raman measurements on the 2D MOFs. The results not only establish their vibrational properties and layer-dependent responses but also show striking differences from other 2D inorganic materials.

Atomically thin layered organic frameworks are a subcategory of 2D materials which can be constructed by coordination bonding of monomers or by inorganic metal clusters and organic linkers to form 2D polymer and 2D metal-organic frameworks (2D MOFs), respectively. These 2D MOFs offer advantages of both 2D layers and traditional MOFs in that they have large surface to volume ratio offering high surface reactivity/sensitivity.^[1] Highly crystalline porous structure within the 2D plane has promising applications in gas sensing and

separation membrane applications.^[2] The presence of transition metal atoms is highly attractive from catalysis and sustainability applications perspective. Lastly, 2D MOFs can be isolated down to monolayers, and owing to their mechanical flexibility they can be implemented into a variety of optoelectronic applications.^[3]

Despite their potential, studies to date show that it is extremely challenging to synthesize and manufacture 2D MOFs at large scales with ultimate control over crystallinity and thickness. Innovative studies by Kitagawa's team have demonstrated that 2D MOF crystal growth (such as NAFS-1 and NAFS-2 nanofilm) takes place at the liquid/air and liquid/liquid interfaces.^[4] Study by Gascon and co-workers developed a three-phase strategy in which metal cation (Cu^{2+}) and organic ligand (carboxyl groups) were localized into two liquid layers and separated by a third layer.^[5] Other complementary methods, such as ultrasonication^[6] and chemical intercalation,^[7] were utilized to yield ultrathin MOFs; however, these

studies only lead to the production of small scale 2D MOFs. As such, many fundamental questions remain open for scalable manufacturing of 2D MOFs. i) How can one attain control over the bonding nature (van der Waals (vdW), hydrogen, or chemical bonding) between layers to produce weakly coupled 2D sheets similar to those in MoS_2 , graphene, and others? ii) How can one optimize the synergistic effect among the metal clusters, ligands, and other reaction additives to avoid the tradeoff between productivity and crystallinity without compromising on its aspect ratio? iii) How to probe fundamental properties of 2D MOF nanosheets through nondestructive methods?

In this work, we have demonstrated the governing effects of interplanar hydrogen bonds induced by coordinated water molecules on the framework dimension (2D vs 3D) of MOF-2. Replacing water with pyridine is a critical piece to attain layered MOF-2D structures while adding controlled amount of triethylamine (TEA) and formic acid allows for tuning kinetic reaction constants by adjusting the proton concentration. Detailed Kelvin probe force microscopy (KPFM) and Raman spectroscopy measurements on these high-quality 2D MOF sheets not

Dr. Y. Shen, B. Shan, Dr. H. Cai, Y. Qin, A. Agarwal, D. B. Trivedi, Dr. B. Chen, L. Liu, Prof. H. Zhuang, Prof. B. Mu, Prof. S. Tongay
School for Engineering of Matter
Transport and Energy
Arizona State University
Tempe, AZ 85287, USA
E-mail: bmu@asu.edu; sefaattintongay@asu.edu



The ORCID identification number(s) for the author(s) of this article can be found under <https://doi.org/10.1002/adma.201802497>.

DOI: 10.1002/adma.201802497

only establish their vibrational properties for the first time, but also show striking differences between inorganic 2D sheets (dichalcogenides) and 2D-MOFs when material thickness is reduced. These results and established synthesis route enable large-scale strategy to realize the layer-by-layer growth of 2D MOF-2 with high yield and scalability.

Achieving Control over Interlayer Hydrogen Bonds versus vdW Forces: Conventional MOF-2 can be described as a ZnBDC framework consisting of Zn tetrahedral clusters connected by four benzene-1,4-dicarboxylic acid (H_2BDC) via coordination bonds, forming molecular arrangements in 2D landscape. Following Yaghi's original work,^[8] although these repeated units constructed along 2D directions, their layers are stacked onto each other tightly through hydrogen bonding. As such, common thinning-down methods such as mechanical exfoliation, polymer-assisted transfer, and liquid phase exfoliation largely fail to produce large-scale MOF-2 nanosheets with high aspect ratios. For example, the uniform solution (shown as blue liquid in **Figure 1a**) in conventional growth consists of dimethylformamide (DMF), water molecules (pink branches), ligand–terephthalic acid (gray bar), and zinc cluster (blue dots), and the established synthesis involving these precursors simply produces strongly coupled sheets (Figure 1b) that have overall chunky/bulk appearance (labeled HB MOF-2) as shown in Figure 1c.

In order to achieve 2D vdW MOF nanosheets that are weakly coupled through vdW forces, we have developed a novel dimension-controllable growth method. In this method, the goal is to minimize interlayer (out-of-plane) growth and reduce interlayer coupling strength to yield ultrathin vdW layered MOF-2 sheets (Figure 1e), while controlling the in-plane (sheet) growth rate

to achieve high aspect ratio (large size 2D sheets) with high crystallinity. Strategy used for achieving vdW layers relies on replacing precursor H_2O that is used in HB MOF-2 synthesis with pyridine molecules along with rate controlling TEA and formic acid agents. In MOF-2, Zn sits in a square-pyramidal coordination geometry with a coordination number at 5, in which the deprotonated ligands (BDC) occupy four coordination sites and the remaining site is occupied by H_2O . Latter site is the origin for the formation of hydrogen bonding across the layers which in return creates strong coupling and thus chunky morphologies as shown in Figure 1c. To limit the formation of hydrogen bonds and change the interlayer bonding from hydrogen to vdW, our method substitutes H_2O with pyridine molecules (C_5H_5N depicted in red in Figure 1d,e), which has energetically favorable binding energies to Zn (0.92 eV) in comparison to H_2O –Zn bonding (0.51 eV). In parallel, our process utilizes TEA and formic acid agents that have been found to be necessary for high yield synthesis of vdW MOF-2 by controlling the reaction speeds.

Synthesis of vdW-MOF-2 by Water/Pyridine Replacement Route: Overall reaction setup is a biphasic synthesis which includes 1) the upper phase (pink region in Figure 1d) consisting of hexane mixed with TEA (which is displayed as branches in light purple highlighted in red circle) and 2) the bottom phase containing diethylformamide (DEF) solved with metal precursors ($M = Zn$ and Cu) and the ligand (H_2BDC), as well as pyridine (highlighted in red circle). In comparison to established HB MOF-2 growth, the addition of pyridine itself in the bottom phase was found to be highly effective in producing highly lamellar vdW MOF-2, as shown in Figure 1f and **Figure 2a–c**, which—we argue—is due to the replacement of hydrogen

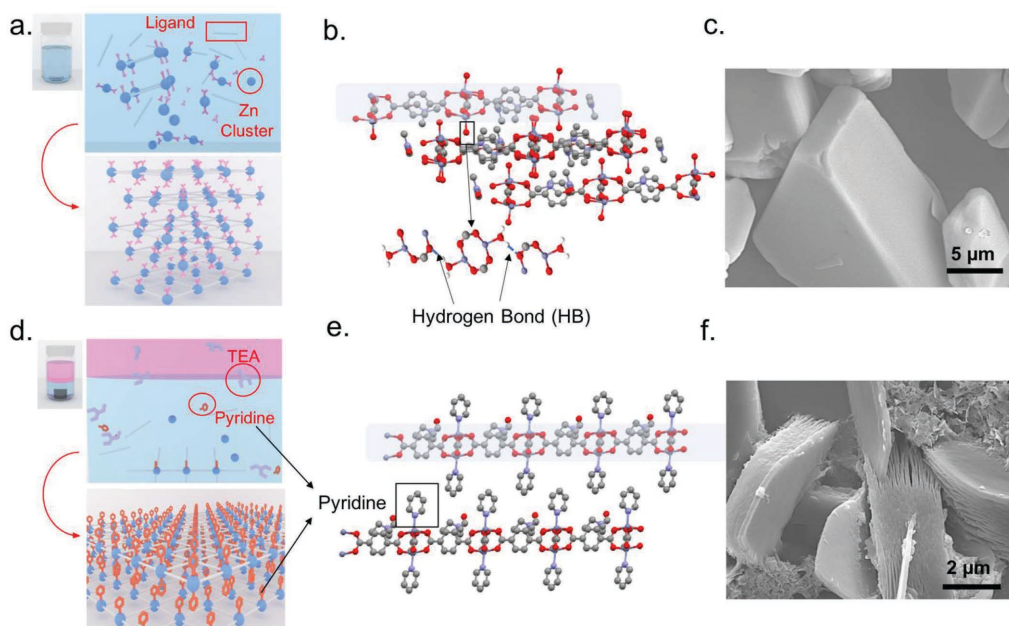


Figure 1. Synthesis routes toward industrially scalable 2D MOF. a) Schematic description of synthesis routes utilized in conventional growth yielding traditional HB MOF-2; b) schematic description of HB MOF-2 and c) SEM image collected from HB MOF-2 materials; d) schematic description of novel biphasic growth of vdW MOF-2; e) these lamellar MOF-2 sheets interact through van der Waals forces (vdW MOF-2) by maximizing the in-plane construction and limiting the out-of-plane growth rates (see depiction) and f) SEM image clearly shows highly lamellar nature of these vdW MOF-2 materials.

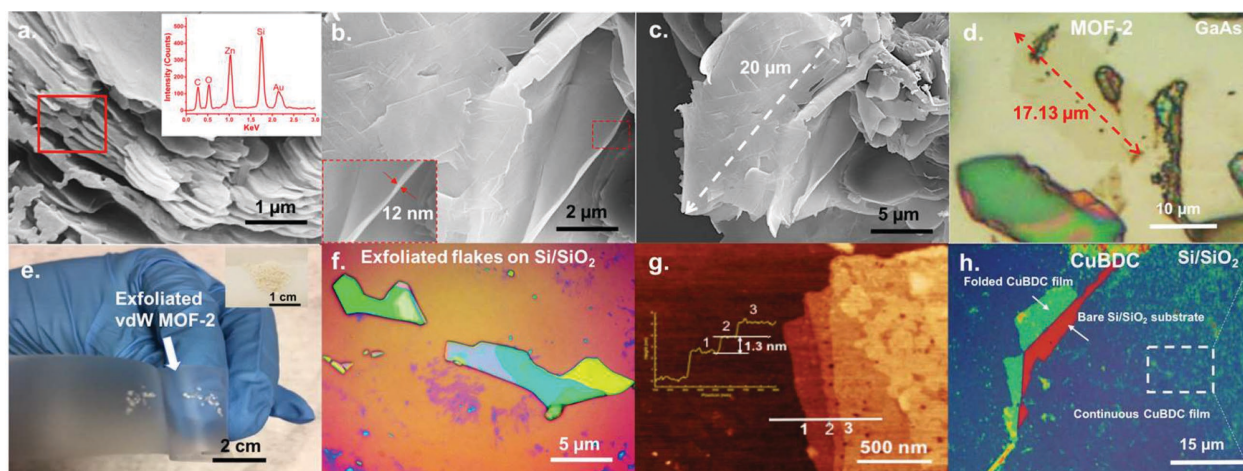


Figure 2. Growth and morphology of vdW MOF-2 and Cu(BDC) nanosheets. a–d) Deposited vdW MOF-2 sheets appear lamellar/layered (a), exhibit smooth surfaces with thickness 10 nm and lower (b), and reach large lateral single-crystal sizes (c,d). e–g) Large crystals of vdW MOF-2 can be attained/collected at the bottom of the reaction vial (e), and these crystals can easily be exfoliated using the standard Scotch tape method (f) onto any arbitrary substrates to yield even monolayer-thick vdW MOF-2 sheets as shown by our AFM measurements (g). h) The technique can be applied to synthesize bulk crystals or even to deposit thin films, as shown by our optical image for CuBDC film grown on substrates. Corresponding EDX data are inserted in (a).

bonds with pyridine molecules around metal sites and reduction of interlayer forces. When replaced, it effectively reduces the hydrogen bond nature, but increases the interlayer separation by linking large pyridine molecule to these metal sites and sustains vdW interactions. This point is clarified later in the article.

The elemental composition of vdW MOF-2 is confirmed by the corresponding energy-dispersive X-ray spectroscopy (EDX) (Figure 2a) wherein silicon and partial oxygen contribution comes from the underlying Si/SiO₂ solid substrates. This method can be used for the synthesis of bulk vdW MOF-2 crystals (Figure 2e) which is naturally collected at the bottom of the reaction vial or in thin film form which can easily be deposited onto any arbitrary substrate. Bulk vdW MOF-2 crystals easily reach gram scales (Figure 2e, inset) and even scaled to larger volumes by simply increasing the overall volume of the precursors. Synthesized bulk vdW MOF-2 shows striking similarities to lamellar h-BN, graphite, or MoS₂ crystals in which they can easily be exfoliated using Scotch tape (Figure 2e) to yield monolayers (see atomic force microscopy (AFM) images in Figure 2g) on arbitrary substrates such as indium tin oxide (ITO)-coated glass or transparent sapphire which will be used for Kelvin probe force microscopy and optical measurements later in the article (Figure 2d–g). After adjusting reaction speeds by TEA and formic acid chemistry (see below), deposited vdW MOF-2 sheets can reach full coverage on substrates as shown in Figure S11a,b (Supporting Information) which is critical for their meaningful applications. Even low-magnification SEM images are sufficient to observe extremely thin lamellar sheets (≈ 10 nm) which comfortably reach up to 10 s of μm and lateral sizes (Figure 2b,c). Such obtained MOF-2 with extremely high aspect ratio ($>10^3$) is a direct evidence of the dimension-control-lable stacking behavior.

Control over Aspect Ratio and Crystallinity by TEA/Formic Acid Chemistry: Here, we note that large-area coverage vdW MOF-2 deposition or highly crystalline bulk vdW MOF-2 largely depends on our ability to control the reaction speeds. For example, without using TEA or formic agents, pyridine alone

only produces very low yield (limited) synthesis of bulk vdW MOF-2 crystals (Section S.1.1, Supporting Information).

We have performed ≈ 200 independent measurements/systematic growth studies to reach fundamental understanding of how addition or concentration of formic acid, TEA, hexane, and other factor influence the growth kinetics. Scalable manufacturing of MOFs typically requires high reactant concentration synthesis to avoid high volumes of solvent. It has been reported that uncontrolled MOF growth in such a condition would lead to amorphous products since the overspeed coordination reaction limits the framework reparation.^[9] Therefore, traditionally the high crystallinity of MOFs is obtained with the sacrifice of production yield.^[10] Similar to traditional MOFs, in-plane construction of MOF-2 involves coordination reaction between organic ligands (dissociated BDC) and metal cations in solution. In this solution, rates are determined by the dissociated proton concentration (c_{H^+}) and control over c_{H^+} is essential to achieve highly crystalline MOF-2.^[11]

Here, we increased c_{H^+} by utilizing formic acid (HCO₂H) in the reaction solution (bottom phase) to effectively reduce the reaction speed as established in our control measurements (Section S.1.2, Supporting Information). Meanwhile, increasing c_{H^+} may also lead to early termination of in-plane growth potentially causing small size MOF-2 crystallites.^[12] To circumvent this problem, we added a deprotonating agent triethylamine (i.e., N(CH₂CH₃)₃) in the upper hexane phase (Figure 1d, pink phase) which has been successfully shown to be effective in increasing the reaction speeds (Section S.1.3, Supporting Information). As TEA diffuses into the bottom phase, it governs the quantity of proton in a direction where TEA diffuses.^[13] Here, hexane also buffers the contact between formic acid and TEA, in that way we have the high crystallinity and yield all at the same time, and optimizing the hexane amount is of paramount importance in the growth process as shown in Section S.1.4 (Supporting Information). Hexane amount is an important synthesis parameter. In this sense, TEA and formic acid agents act as gas and brake pedal for the reaction and control the

overall growth speed. Since coordination reaction takes place in an environment with strictly defined proton concentration, this biphasic method gives birth to the scalable synthesis of 2D MOFs. We also point out that mixing formic acid and TEA in a single phase solution while producing vdW MOF-2 also sacrifices the yield as well as the crystallinity. Thus, our studies show that it is necessary to separate these two counteracting agents into two phases as demonstrated in Section S.1.5 (Supporting Information). Overall, all above parameter influences the growth kinetics and outcome and careful optimization is needed to achieve large size crystallites as demonstrated in Section S.1.6 in the Supporting Information.

The novel biphasic growth method described here has several advantages over other established 2D MOF growth routes. First, our method replaces water with pyridine and reduces the hydrogen formation intentionally, and produces vdW MOF-2 sheets. Based on our exploratory studies, it can also be applied to—at the very least—Cu(BDC) (Figure 2h; Figure S11c,d, Supporting Information).^[14] Second, the formic acid and gradient TEA along the bottom reaction phase offer effective control over proton concentration as well as the quantity of partially deprotonated ligand (see Section S.1 in the Supporting Information all together). This growth mechanism offers the capacity for scalable synthesis of 2D MOFs without sacrificing the crystallinity as evidenced by full width at half maximum (FWHM) Raman spectrum analysis that is detailed in the next section. The overall yield can reach 71% in the synthesis of vdW MOF-2 and 80% in CuBDC, respectively. To the best of our knowledge, such high yield of 2D MOFs is remarkable in published bottom-up methods.^[15]

Fundamental Insights on vdW MOF-2 Structure: While electron diffraction techniques allow for direct ways to confirm this crystalline structure, our extensive scanning transmission electron microscopy (STEM), transmission electron microscopy (TEM), and cryo-TEM measurements were shown to be ineffective due to damage threshold far below 60 keV. To shed light into the structure of MOF-2, we have constructed and relaxed vdW MOF-2 unit cell (Figure 3a) using density functional theory, calculated the expected X-ray diffraction (XRD) as well as vibrational spectrum (Raman spectrum). Results were compared to experimental data (Figure 3b) and both theory and experimental results were iterated a number of times until good match in calculated and measured XRD and Raman spectrum was achieved.

To show the efficacy of the approach, we have first calculated the diffraction pattern of refined HB MOF-2 unit cell which was found to be consistent with prior literature^[16] and compared it to our experimental HB MOF-2 datasets. Striking similarities between these two datasets (dark green and yellow) are shown in Figure 3b (green). Using similar methodologies, similar comparisons were made for vdW MOF-2 first by constructing and relaxing the vdW MOF-2 structure (Figure S12, Supporting Information). Resulting vdW MOF-2 structure is shown in Figure 3a (in-plane and side views); comparison between theoretical XRD patterns (black solid line) and experimental datasets acquired from synthesized vdW MOF-2 (red solid lines) are shown in Figure 3b. First, experimental XRD data collected from HB (green) and vdW (red) MOF-2 show differences mostly related to out-of-plane distance differences which is further clarified below. Similarly, Cu(BDC) vdW layers also exhibit

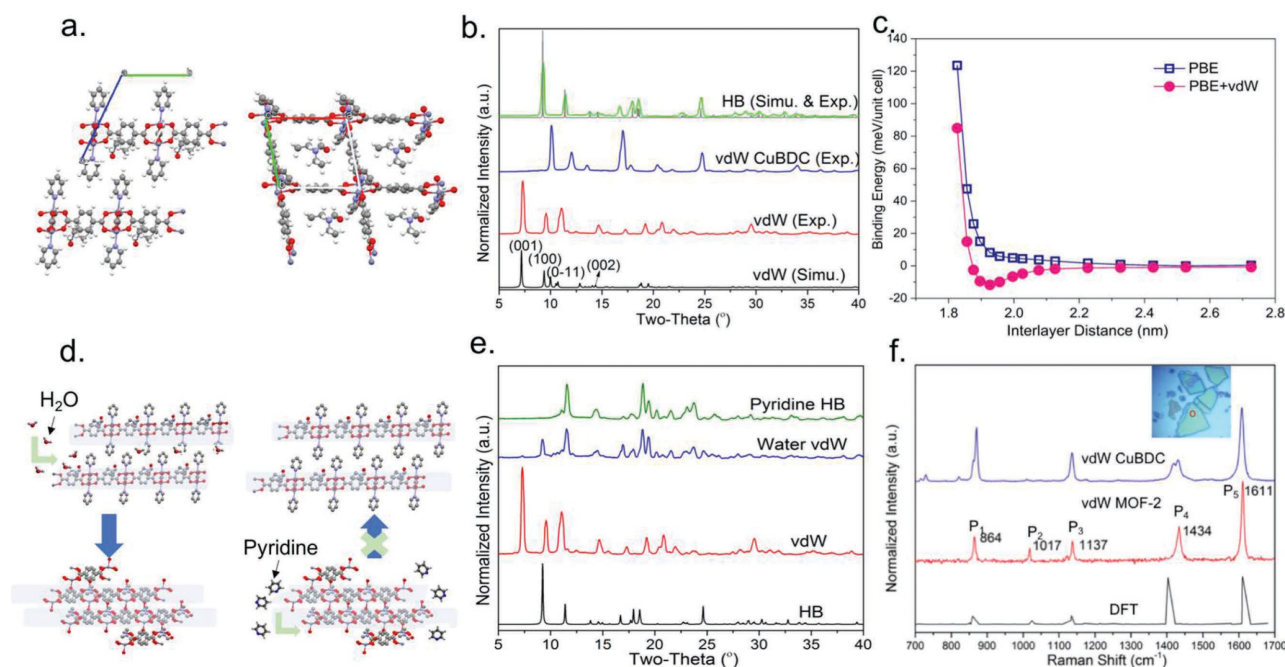


Figure 3. Structural and vibrational properties of 2D vdW MOF-2. a) Refined structure of vdW MOF-2; b) powder XRD patterns of HB MOF-2 (experimental and simulated) and vdW MOF-2 (experimental and simulated) as well as vdW Cu(BDC); c) interlayer binding energy calculated by DFT; d,e) vdW MOF-2 samples soaked under water under irreversible transformation from vdW to HB due to pyridine–water replacement mechanism. f) Micro-Raman spectra of vdW MOF-2 (ZnBDC), as well as DFT simulation results, respectively, and inserted optical images of MOF-2 and CuBDC with white spots show the locations where micro-Raman spectra are measured.

similar prominent peaks but at different positions due to different lattice spacings originating from Cu and Zn clusters.

A closer look at the calculated and experimental XRD patterns of vdW MOF-2 shows confirmed 00l reflections related to reflections from adjacent vdW layers, and most of the prominent peaks can be closely matched to those simulated ones. 2θ values are as close as $\approx 0.4^\circ$. We also note that vdW MOF-2 is indeed lamellar in nature as evidenced by DFT binding energy calculations: plotting interlayer binding energy with respect to interlayer distance shows that energetic minima (stable stacking) can only be attained by vdW functional corrections that are incorporated into DFT calculations (Figure 3c).

Here, to further demonstrate the similarities between HB and vdW MOF-2 structures, we have immersed vdW MOF-2 sheets under ultrapure H_2O for 24 h. Our results show that vdW MOF-2 structure successfully transitions from vdW like to HB like (Figure 3d) which means that H_2O molecules effectively diffuse between the layers and replace pyridine groups with H_2O . We note that large crystal structure changes are highly unlikely since the process itself is limited to room temperature. This process also offers an evidence that pyridine molecules originally sit where hydrogen bonds are positioned since interaction with H_2O simply reduces vdW into HB MOF-2 (see schematic in Figure 3d and XRD datasets in Figure 3e). This chemical reaction is unidirectional since drying transformed HB MOF-2 does not reverse the structure (Figure 3d).

Vibrational Dispersion and Raman Spectrum: Further structural confirmation was obtained by comparing calculated vibrational spectrum (simulated Raman spectrum) to experimental Raman spectrum in Figure 3f. The black solid line in Figure 3f represents simulated Raman spectrum coming from DFT calculations near $\Gamma = 0$ point which displays a close resemblance to our experimental results (red solid line). Observed close agreements between calculated XRD, vibrational spectrum, and our experimental results convincingly demonstrate that anticipated structure is accurate. Our detailed angle-resolved Raman measurements on vdW as well as HB MOF-2 structures also show further evidence for proposed structure as well as crystallinity in Figures S13 and S14 (Supporting Information). Here, we note that while Raman spectrum analysis has been successfully applied to many inorganic 2D crystals, previous studies failed to apply this method to vdW MOFs due to limitations in synthesis methods to achieve larger area nanosheets with high crystallinity, and our work introduces this technique for vdW MOF-2.

Typical Raman spectrum collected from MOF-2 sheets exhibited five prominent peaks with low FWHM ($\approx 6\text{ cm}^{-1}$), located at 864, 1017, 1137, 1434, and 1611 cm^{-1} and marked as P_1 , P_2 , P_3 , P_4 , and P_5 , respectively (Figure 3f). Rather low Raman FWHM values suggest that the defect concentration is low and most of the phonon vibration modes only come around the $\Gamma = 0$ point due to Raman selection rules. This means that resulting materials exhibit high crystallinity though intrinsic point defect concentration remains unknown currently. Finite displacement analysis was also performed to extract out the atomic vibrational character of predicted modes which has been outlined in Table 1. Here, P_4 peak position shows appreciable disagreement between predicted and measured Raman peak positions. Since this mode is related to atomic vibrations around Zn clusters

Table 1. Description of atomic vibrations involving Raman active modes in vdW MOF-2.

	Location [cm^{-1}]	Vibration modes
P_1	864	Zn cluster breathing, benzene ring contracting, and C–H stretching (new in 2D MOFs)
P_2	1017	Pyridine ring breathing and C–H stretching (pyridine related)
P_3	1137	Benzene bending and C–H stretching (ligand related)
P_4	1434	Zn cluster contracting and C–H bending in DEF (new in 2D MOFs and DEF related partially)
P_5	1611	Benzene ring breathing and C–H bending (ligand related)

and C–H bending in DEF, we attribute this slight discrepancy to a deviation from local force field generated from the interaction between solvent and MOF network.

While it is clear that FWHM, peak position, as well as Raman line-shapes allow us to distinguish crystallized vdW MOF from constituent chemicals, it is essential to also develop guidelines for recognizing different types of vdW MOFs from simple and nondestructive Raman measurements. Close comparison between vdW Cu (CuBDC, blue curve) and Zn-based vdW MOFs (MOF-2, red curve) shows three striking differences between these two materials: 1) P_1 and P_4 peaks located at 864 and 1434 cm^{-1} split and shift in CuBDC vdW MOFs in comparison to MOF-2. Interestingly, these two modes are made of atomic vibrations involving metal clusters as listed in Table 1. This finding is quite reasonable since atomic weight directly influences vibration frequencies of these modes. As such, these effects manifest it in terms of different peak positions as well as line shapes as observed in Figure 3f, and P_1/P_4 peaks can be used as material type identification.

Additionally, the Raman spectra of MOF-2 and CuBDC vdW layers are compared to constituent chemicals such as DEF, H_2BDC , and pyridine to understand the contributions arising from these chemicals to the overall Raman spectra (Figure S15, Supporting Information). While observed Raman peaks of vdW MOFs show distant resemblances to H_2BDC and DEF, well-crystallized vdW exhibit peaks that are much more intense, well-defined, and are located at different frequencies. For example, in comparison to H_2BDC and DEF, C–C breathing mode (P_5 mode) becomes much sharper ($45\text{ cm}^{-1} \rightarrow 6\text{ cm}^{-1}$) after vdW MOF is crystallized. Also, $P_{1,2,3,4}$ peaks are generally blueshifted due to the formation of new bonds and have different Raman line-shapes.

Thickness-Dependent Behavior: Reduced interlayer coupling and vdW nature of these synthesized sheets enabled us to perform thickness-dependent material properties for the first time. In past, small lateral size and strong hydrogen bonding between the layers limited our ability to shed light on their material behavior at nanoscales which is precisely why the literature predominantly focuses on the bulk material behavior instead of ultrathin 2D response. Due to their low electronic optical activity, we have performed KPFM measurements to probe their surface potential values as a gauge for material behavior. Previously, the KPFM technique has been applied in graphene and other 2D systems as a successful tool to probe spatial distribution of charge carriers as well as interlayer

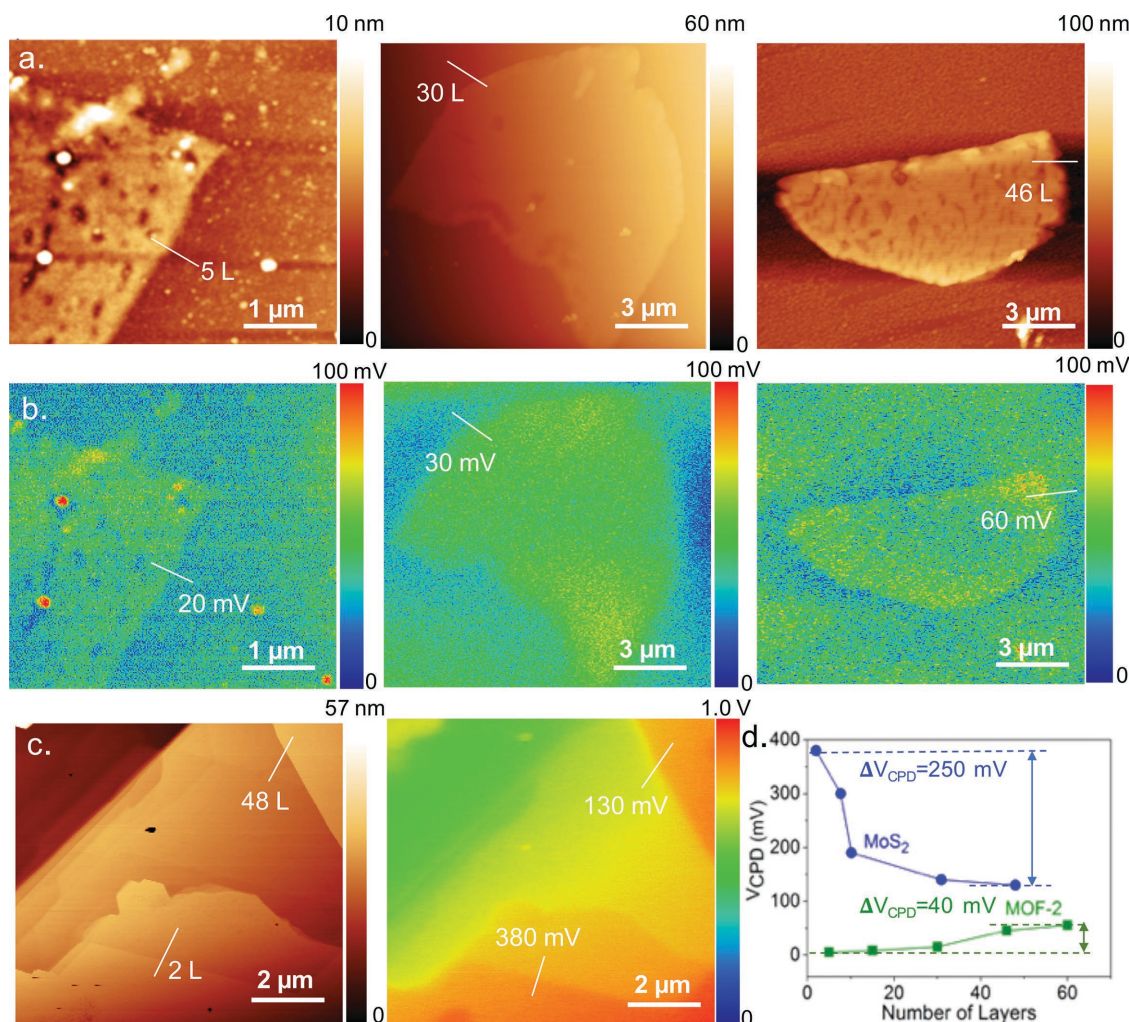


Figure 4. Kelvin probe force microscopy for thickness-dependent phenomena. a) AFM images and b) KPFM scans of vdW MOF-2 sheets deposited onto conductive ITO substrates; c) AFM and KPFM scans on exfoliated MoS₂ sheets onto conductive ITO; d) change in V_{CPD} with respect to sheet thickness for vdW MOF-2 and MoS₂.

screening effect by measuring the surface potential of 2D material with varied thickness.^[17] We have performed a series of KPFM studies on synthesized vdW MOFs and compared their thickness response to that from mechanically exfoliated molybdenum disulfide (MoS₂), a well-known 2D semiconductor, as a reference (Figure 4).

Here, the work function is determined by $\phi_{\text{tip}} - qV_{\text{CPD}} = \phi_{\text{sample}}$, where ϕ_{tip} is the work function of the AFM tip (5.25 eV), q is the electron charge, and V_{CPD} is the contact potential difference measured by KPFM. As shown in Figure 4c, the surface potential of MoS₂ shows dramatic variation with thickness (ranging from 1 nm to several tens of nanometers) which is consistent with the previously published results.^[18] The origin of this surface potential variation has been attributed to the partially overlapped d orbitals of Mo and p orbitals of S atoms across adjacent layers which is related to how well or poorly the layers are coupled to each other.

In contrast, the surface potential distribution of 2D vdW MOF-2 (Figure 4a,b) appears uniform across the flake and independent of thickness with a value of 3.22 V. These values show

only small change from 20 to 60 mV ($\Delta V_{\text{CPD}} \approx 40$ mV) from 46L down to 5L which is minuscule comparing to traditional inorganic vdW 2D materials. In MoS₂, for example, ΔV_{CPD} is 250 mV from 2 to 48 layers and 180 mV from 5 to 48 layers. These measurements were repeated on a variety of samples from different batches and similar results were observed. The absence of thickness dependence of the work function may be explained by the electron charge density distribution in layered MOF-2: as shown in Figure S16 (Supporting Information), the benzene rings in MOF-2 are all perpendicular to the plane, so the π bonds formed by p orbitals of carbon atom are extended in-plane and do not overlap between the two layers. This is in stark contrast to other 2D carbonaceous materials like graphene where interlayer coupling predominantly occurs through C atoms' p orbital interaction in adjacent layers. Despite these findings, we still anticipate that constituent layers in vdW MOFs are still coupled to each other much similar to other 2D vdW crystals. However, KPFM surface potential measurements alone show that the interaction is not strong enough to cause sizable changes in the surface potential values of vdW MOFs.

While interlayer coupling might be weak, how the interactions between the vdW MOF layers influence material behavior warrant future studies.

Summary: We have demonstrated a scalable and reproducible biphasic synthesis method for large-scale high quality production of vdW MOFs sheets. Replacing water molecules with pyridine has been identified as the primary factor sustaining perfectly layered vdW MOF sheets. At the same time, addition of TEA and formic acid deprotonating and protonating agents have been found to be highly effective in increasing and slowing down the chemical reaction rates and growth speeds to attain highly crystalline vdW MOF sheets which has been evidenced by SEM, EDX, AFM, and optical images, and confirmed by detailed Raman spectroscopy measurements. Owing to large lateral sizes, vdW nature, and high crystallinity, we were able to perform AFM, KPFM, and Raman measurements to establish their fundamental vibrational properties as novel material characterization tool, while providing the very first insight on their thickness-dependent properties. Overall findings are anticipated to open up new avenues toward large-scale synthesis of vdW MOFs by offering ways to manipulate interlayer coupling strength and reaction rates, and offer fundamental insights into their vibrational and thickness-dependent properties.

Experimental Section

Biphasic Synthesis of vdW MOF-2: $\text{Zn}(\text{NO}_3)_2 \cdot 6\text{H}_2\text{O}$, $\text{Cu}(\text{NO}_3)_2 \cdot 3\text{H}_2\text{O}$, benzene-1,4-dicarboxylic acid (H_2BDC), pyridine, triethylamine, hexane, formic acid, isopropanol, and acetone were purchased from Sigma-Aldrich without further purification. *N,N*-Dimethylformamide and *N,N*-diethylformamide were purchased from Fisher Scientific. For the biphasic system, formic acid (0.04 mL), $\text{Zn}(\text{NO}_3)_2 \cdot 6\text{H}_2\text{O}$ (0.18 mmol), pyridine (0.02 mL), and H_2BDC (0.1 mmol) were dissolved in 5 mL of DEF to form the bottom solution. And the upper solution was formed by adding TEA (0.07 mL) to 5 mL of hexane. After all the components are dissolved, the bottom solution was slowly injected underneath upper one. This two-phase system was sealed in a glass vial and kept at room temperature for 24 h. For the growth of vdW MOF-2 on substrates, the selected substrates were held by a Teflon supporter and placed in the DEF phase vertically. The same recipe was also applied to grow CuBDC except the $\text{Zn}(\text{NO}_3)_2 \cdot 6\text{H}_2\text{O}$ was replaced with the same mole of $\text{Cu}(\text{NO}_3)_2 \cdot 3\text{H}_2\text{O}$. Samples collected from vials were undergone activation by immersing in 10 mL of acetone for 3 days and drying in vacuum at 120 °C for 12 h. In water intercalation, 50 mg of vdW MOF-2 was placed in 10 mL of ultrapure water for 24 h. Then, the sample was dried in fume hood. In pyridine intercalation, 50 mg of HB MOF-2 was placed in 10 mL of pyridine for 24 h. Then, the sample was dried in fume hood.

Conventional Synthesis of HB MOF-2: The conventional synthesis of MOF-2 was extensively reported, here it is referred to as Manuel's publication^[9]: $\text{Zn}(\text{OAc})_2 \cdot 2\text{H}_2\text{O}$ of 1.56 g (7.24 mmol) was dissolved in 11.04 mL (0.61 mol) of water and 0.68 g (4.1 mmol) H_2BDC was dissolved in 14.18 mL of DMF. The blended solution under continuous stirring formed white precipitates within 15 min, and the suspension remained under stirring at room temperature for 24 h. The precipitate was then filtered and washed repeatedly with DMF and dried overnight.

Characterization: The morphologies of vdW MOF-2 and CuBDC were observed with a Philips XL30 environmental scanning electron microscope at a voltage of 10 kV with the assistance of Au sputter coating. The Raman spectroscopy measurements were taken using a Renishaw InVia Raman microscope under 100 objective lens using 488 nm laser as the excitation source, and the laser power was set to 37.5 μW .

Ingredients, including H_2BDC , DEF, and pyridine, were measured from powder samples purchased from Sigma. Topography and electrical measurements were both conducted by a Bruker Multimode 8 instrument with a Nanoscope V controller. Samples were mounted on an ITO substrate for electrical measurements. Silver or nickel paste was used to connect the ITO surface to a sample mounting disk. Surface potential was measured in an amplitude modulation mode with a Au-coated probe. The work function of the tip was calibrated by scanning the freshly exfoliated highly ordered pyrolytic graphite. Pt/Ir-coated tips were used for conductive AFM measurements in the contact mode. The scanning size was 256×256 , and the scanning speed was set to 1 Hz. Data were analyzed by Gwyddion software and MATLAB. The XRD of samples was collected using a Bruker D8 ADVANCE powder diffractometer with $\text{Cu K}\alpha$ radiation ($\lambda = 1.542$) at 40 kV and 40 mA and scan step of 0.02° .

Theoretical Predictions: We used the Vienna ab initio Simulation Package (VASP)^[20] to perform density functional theory (DFT) calculations. We also adopted the Perdew–Burke–Ernzerhof^[21] (PBE) functional for treating the electron–electron exchange–correlation interactions. Correspondingly, we used the PBE version of potential datasets generated according to the projector augmented wave^[22] (PAW) method, where the 1s state of H, $2s^2 2p^2$ states of C, $2s^2 2p^3$ states of N, $2s^2 2p^4$ states of O, and $3d^{10} 4s^2$ states of Zn were accounted for as valence electrons. The cutoff energy for the plane wave basis sets was set to 500 eV. For the *k*-point sampling, we used a $2 \times 2 \times 1$ grid for the MOF supercells with and without a pyridine molecule. A vacuum spacing of more than 25.0 Å was used to separate the image interactions of each supercell due to the periodic boundary conditions. Before analyzing the electronic structure and computing the Raman spectrum, geometry optimizations were performed until the total energy and force was converged to 10^{-6} eV and $0.01 \text{ eV } \text{\AA}^{-1}$, respectively. The calculations of Raman spectrum were based on the method by Porezag and Pederson.^[23]

Supporting Information

Supporting Information is available from the Wiley Online Library or from the author.

Acknowledgements

Y.S. and B.S. contributed equally to this work. B.M. would like to acknowledge funding from National Science Foundation (Grant No. CBET-1748641 and CMMI-1825594). L.L. and H.L.Z. thank the start-up funds from Arizona State University. This work also used computational resources of Texas Advanced Computing Center under Contract No. TG-DMR170070. S.T. acknowledges support from NSF CMMI-1825594 and DMR-1552220. The authors acknowledge the use of facilities within the Eyring Materials Center at Arizona State University supported in part by NNCI-ECCS-1542160.

Conflict of Interest

The authors declare no conflict of interest.

Keywords

crystallinity, hydrogen bonds, reaction rate, scalable synthesis, vdW 2D MOFs

Received: April 18, 2018

Revised: October 6, 2018

Published online: November 2, 2018

- [1] a) M. Zhao, Y. Wang, Q. Ma, Y. Huang, X. Zhang, J. Ping, Z. Zhang, Q. Lu, Y. Yu, H. Xu, Y. Zhao, H. Zhang, *Adv. Mater.* **2015**, 27, 7372; b) G. Hai, X. Jia, K. Zhang, X. Liu, Z. Wu, G. Wang, *Nano Energy* **2018**, 44, 345.
- [2] a) Z. Kang, L. Fan, D. Sun, *J. Mater. Chem. A* **2017**, 5, 10073; b) Y. Peng, Y. Li, Y. Ban, W. Yang, *Angew. Chem.* **2017**, 56, 9757; *Angew. Chem., Int. Ed.* **2017**, 56, 9757.
- [3] a) A. K. Chaudhari, H. J. Kim, I. Han, J.-C. Tan, *Adv. Mater.* **2017**, 29, 1701463; b) D. Feng, T. Lei, M. R. Lukatskaya, J. Park, Z. Huang, M. Lee, L. Shaw, S. Chen, A. A. Yakovenko, A. Kulkarni, J. Xiao, K. Fredrickson, J. B. Tok, X. Zou, Y. Cui, Z. Bao, *Nat. Energy* **2018**, 3, 30; c) A. Sengupta, S. Datta, C. Su, T. S. Herng, J. Ding, J. J. Vittal, K. P. Loh, *ACS Appl. Mater. Interfaces* **2016**, 8, 16154; d) V. Stavila, A. A. Talin, M. D. Allendorf, *Chem. Soc. Rev.* **2014**, 43, 5994.
- [4] a) S. Motoyama, R. Makiura, O. Sakata, H. Kitagawa, *J. Am. Chem. Soc.* **2011**, 133, 5640; b) R. Makiura, S. Motoyama, Y. Umemura, H. Yamanaka, O. Sakata, H. Kitagawa, *Nat. Mater.* **2010**, 9, 565.
- [5] T. Rodenas, I. Luz, G. Prieto, B. Seoane, H. Miro, A. Corma, F. Kapteijn, F. X. Llabrés i Xamena, J. Gascon, *Nat. Mater.* **2015**, 14, 48.
- [6] P. Amo-Ochoa, L. Welte, R. Gonzalez-Prieto, P. J. Sanz Miguel, C. J. Gomez-Garcia, E. Mateo-Marti, S. Delgado, J. Gomez-Herrero, F. Zamora, *Chem. Commun.* **2010**, 46, 3262.
- [7] P.-Z. Li, Y. Maeda, Q. Xu, *Chem. Commun.* **2011**, 47, 8436.
- [8] H. Li, M. Eddaoudi, T. L. Groy, O. M. Yaghi, *J. Am. Chem. Soc.* **1998**, 120, 8571.
- [9] a) M. J. V. Vleet, T. Weng, X. Li, J. R. Schmidt, *Chem. Rev.* **2018**, 118, 3681; b) B. Bueken, N. V. Velthoven, T. Willhammar, T. Stassin, I. Stassen, D. A. Keen, G. V. Baron, J. F. M. Denayer, R. Ameloot, S. Bals, D. D. Vos, T. D. Bennett, *Chem. Sci.* **2017**, 8, 3939.
- [10] G. Zahn, P. Zerner, J. Lippke, F. L. Kempf, S. Lilienthal, C. A. Schroder, A. M. Schneider, P. Behrens, *CrystEngComm* **2014**, 16, 9198.
- [11] a) H. Guo, Y. Zhu, S. Wang, S. Su, L. Zhou, H. Zhang, *Chem. Mater.* **2012**, 24, 444; b) D. Feng, K. Wang, Z. Wei, Y.-P. Chen, C. M. Simon, R. K. Arvapally, R. L. Martin, M. Bosch, T.-F. Liu, S. Fordham, D. Yuan, M. A. Omary, M. Haranczyk, B. Smit, H.-C. Zhou, *Nat. Commun.* **2014**, 5, 5723; c) R. Nayuk, D. Zacher, R. Schweins, C. Wiktor, R. A. Fischer, G. V. Tendeloo, K. Huber, *J. Phys. Chem. C* **2012**, 116, 6127.
- [12] D. Zacher, R. Nayuk, R. Schweins, R. A. Fischer, K. Huber, *Cryst. Growth Des.* **2014**, 14, 4859.
- [13] B. Shan, J. B. James, M. R. Armstrong, E. C. Close, P. A. Letham, K. Nikkiah, Y. S. Lin, B. Mu, *J. Phys. Chem. C* **2018**, 122, 2200.
- [14] a) Y. Yang, K. Goh, R. Wang, T.-H. Bae, *Chem. Commun.* **2017**, 53, 4254; b) C. Kutzscher, A. Gelbert, S. Ehrling, C. Schenk, I. Senkovska, S. Kaskel, *Dalton Trans.* **2017**, 46, 16480.
- [15] a) Y. Ding, Y.-P. Chen, X. Zhang, L. Chen, Z. Dong, H.-L. Jiang, H. Xu, H.-C. Zhou, *J. Am. Chem. Soc.* **2017**, 139, 9136; b) K. Zhao, S. Liu, G. Ye, Q. Gan, Z. Zhou, Z. He, *J. Mater. Chem. A* **2018**, 6, 2166.
- [16] H. Furukawa, K. E. Cordova, M. O. Keeffe, O. M. Yaghi, *Science* **2013**, 341, 1230444.
- [17] a) S. S. Datta, D. R. Strachan, E. J. Mele, A. T. C. Johnson, *Nano Lett.* **2009**, 9, 7; b) R. Vidyasagar, B. Camargo, K. Romanyuk, A. L. Kholkin, *Ferroelectrics* **2017**, 508, 115.
- [18] Y. Li, C.-Y. Xu, L. Zhen, *Appl. Phys. Lett.* **2013**, 102, 143110.
- [19] N. Getachew, Y. Chebude, I. Diaz, *J. Porous Mater.* **2014**, 21, 769.
- [20] a) G. Kresse, J. Furthmüller, *Comput. Mater. Sci.* **1996**, 6, 15; b) G. Kresse, J. Furthmüller, *Phys. Rev. B* **1996**, 54, 11169.
- [21] J. P. Perdew, K. Burke, M. Ernzerhof, *Phys. Rev. Lett.* **1996**, 77, 3865.
- [22] a) P. E. Blöchl, *Phys. Rev. B* **1994**, 50, 17953; b) G. Kresse, D. Joubert, *Phys. Rev. B* **1999**, 59, 1758.
- [23] D. Porezag, M. R. Pederson, *Phys. Rev. B* **1996**, 54, 7830.